OPEN ACCESS
IOP Publishing

Made open access 22 July 2016
Plasma Sources Science and Technology

Plasma Sources Sci. Technol. **25** (2016) 045015 (17pp)

doi:10.1088/0963-0252/25/4/045015

Electron power absorption dynamics in capacitive radio frequency discharges driven by tailored voltage waveforms in CF_4

S Brandt[1], B Berger[1,2], E Schüngel[1], I Korolov[3], A Derzsi[3], B Bruneau[4], E Johnson[4], T Lafleur[5], D O'Connell[6], M Koepke[1], T Gans[6], J-P Booth[5], Z Donkó[3] and J Schulze[1,2]

[1] Department of Physics, West Virginia University, Morgantown, WV 26506-6315, USA
[2] Institute for Electrical Engineering, Ruhr-University Bochum, D-44780 Bochum, Germany
[3] Institute for Solid State Physics and Optics, Wigner Research Centre for Physics, Hungarian Academy of Sciences, 1121 Budapest, Konkoly-Thege Miklós str. 29-33, Hungary
[4] LPICM-CNRS, Ecole Polytechnique, Université Paris-Saclay, 91128 Palaiseau, France
[5] LPP-CNRS, Ecole Polytechnique, Université Paris-Saclay, 91128 Palaiseau, France
[6] York Plasma Institute, Department of Physics, University of York, Heslington, York, YO10 5DD, UK

E-mail: sbrandt1@mix.wvu.edu

Received 12 February 2016
Accepted for publication 11 April 2016
Published 29 June 2016

Abstract

The power absorption dynamics of electrons and the electrical asymmetry effect in capacitive radio-frequency plasmas operated in CF_4 and driven by tailored voltage waveforms are investigated experimentally in combination with kinetic simulations. The driving voltage waveforms are generated as a superposition of multiple consecutive harmonics of the fundamental frequency of 13.56 MHz. Peaks/valleys and sawtooth waveforms are used to study the effects of amplitude and slope asymmetries of the driving voltage waveform on the electron dynamics and the generation of a DC self-bias in an electronegative plasma at different pressures. Compared to electropositive discharges, we observe strongly different effects and unique power absorption dynamics. At high pressures and high electronegativities, the discharge is found to operate in the drift-ambipolar (DA) heating mode. A dominant excitation/ionization maximum is observed during sheath collapse at the edge of the sheath which collapses fastest. High negative-ion densities are observed inside this sheath region, while electrons are confined for part of the RF period in a potential well formed by the ambipolar electric field at this sheath edge and the collapsed (floating potential) sheath at the electrode. For specific driving voltage waveforms, the plasma becomes divided spatially into two different halves of strongly different electronegativity. This asymmetry can be reversed electrically by inverting the driving waveform. For sawtooth waveforms, the discharge asymmetry and the sign of the DC self-bias are found to reverse as the pressure is increased, due to a transition of the electron heating mode from the α-mode to the DA-mode. These effects are interpreted with the aid of the simulation results.

Keywords: voltage waveform tailoring, multi-frequency capacitive discharges, electronegative plasmas, electrical asymmetry effect

(Some figures may appear in colour only in the online journal)

1. Introduction

Optimal utilization of technological plasmas, such as those used in plasma medicine [1–3] or the plasma etching of semiconductors [4, 5], often requires finely tuned local plasma parameters, such as ion fluxes and particle energy distributions at a substrate surface. Customized flux-energy distribution functions for electrons, ions, and neutral radicals in these plasmas are necessary for optimum process control for a variety of applications such as anisotropic dielectric etching, plasma-enhanced chemical vapor deposition (PECVD) [6], etc. Such control is not possible in classical single-frequency capacitively coupled plasmas (CCPs) or single-source inductively coupled plasmas (ICPs) [7–11]. Classical dual-frequency CCPs operated at significantly different frequencies allow for separate control of 'integral quantities' of ion energy distribution functions (IEDFs) such as the mean ion energy and ion flux, but only within a certain window of operating conditions [11–16]. The addition of RF substrate biasing in ICPs allows the average ion energy to be increased in a controlled way.

A promising new way to achieve an advanced control of distribution functions and to improve the plasma's lateral uniformity across large substrates is driving RF plasmas with *tailored voltage waveforms* [17–52]. With this technique, the sheath voltage waveforms as well as the time dependence of the electric field in the sheaths and in the plasma bulk can be customized on a nanosecond timescale. As a consequence, the ion and electron power absorption dynamics can be controlled and distribution functions of different particle species can be customized [17–20, 23–34, 37–39]. Integral quantities, such as the mean ion energies, can then be tailored for various applications. Recently, it was found that even the shape of the IEDF can be controlled using voltage waveform tailoring (VWT) [35, 36]. Johnson *et al* and Schüngel *et al* demonstrated various advantages of using VWT for PECVD [42–45].

Such voltage waveforms can be generated as a superposition consisting of multiple consecutive harmonics of a fundamental driving frequency. These waveforms can be customized by individually adjusting their harmonics' amplitudes and phases. Any driving voltage waveform can be generated in this way using a sufficient number of harmonics. Efficient delivery of such waveforms with impedance matching is possible based on a novel RF supply and matching system [47].

Investigating the effect of the driving voltage waveform on the electron power absorption dynamics (referred to as electron heating dynamics in previous works [25–32, 39, 53–57]) is a crucial step in the fundamental understanding of the way these plasmas are generated. This is the basis for customizing distribution functions of both electrons and ions and, thus, for process optimization based on plasma science. A major stride towards this goal has been the discovery of the electrical asymmetry effect (EAE) in CCPs driven by two consecutive harmonics by Heil *et al* [17]. The EAE includes two effects: the amplitude asymmetry effect (AAE) and the slope asymmetry effect (SAE). The AAE is the generation of a DC self-bias as a function of the phase between the driving harmonics that changes the difference between the global extrema of the driving voltage waveform. The AAE was verified by simulations [18, 20, 22–24, 41] and experiments [19–24, 40, 46], as well as demonstrated to be strongly enhanced by using more than two harmonics [25–34, 37–39, 47, 48]. Later, Bruneau *et al* discovered the slope asymmetry effect (SAE) in argon, which also generates a DC self-bias and induces a discharge asymmetry by using sawtooth-like waveforms with identical global extrema, but with significantly different rise- and fall-times [49–52]. These previous investigations were mostly limited to electropositive plasmas operated in the α-heating mode.

An analytical model of the EAE introduced by Heil *et al* [17] has been described in detail by Czarnetzki *et al* [20]. Based on the individual voltage drops across the sheaths adjacent to each electrode and across the bulk, an expression for the DC self-bias, η, is obtained in this model as [17, 20]:

$$\eta = -\frac{\tilde{\phi}_{\max} + \varepsilon\tilde{\phi}_{\min}}{1+\varepsilon} + \frac{\phi^f_{\rm sp} + \varepsilon\phi^f_{\rm sg}}{1+\varepsilon} + \frac{\phi^b_{\max} + \varepsilon\phi^b_{\min}}{1+\varepsilon}, \qquad (1)$$

where $\tilde{\phi}_{\max}$ and $\tilde{\phi}_{\min}$ are the global maximum and minimum of the applied voltage waveform, $\phi^f_{\rm sp}$ and $\phi^f_{\rm sg}$ are the floating potentials at the powered and grounded electrodes, and $\phi^b_{\max}$ and $\phi^b_{\min}$ are the voltage drops across the bulk at the times of maximum and minimum applied voltage, respectively. The bulk voltage drop $\phi_{\rm b}$ in equation (1) can usually be neglected for electropositive plasmas (e.g. argon) at low pressures [58], but cannot be neglected in the case of electronegative gases (e.g. CF_4), where significant drift electric fields are often present in the plasma bulk and ambipolar fields can be generated near the sheath edges [40, 41, 53, 59–64]. However, even for electronegative plasmas, the applied voltage waveform, i.e. the first term in equation (1) is typically dominant compared to the other terms. The symmetry parameter ε is defined by:

$$\varepsilon = \left|\frac{\phi^{\max}_{\rm sg}}{\phi^{\max}_{\rm sp}}\right| \approx \left(\frac{A_{\rm p}}{A_{\rm g}}\right)^2 \frac{\bar{n}_{\rm sp}}{\bar{n}_{\rm sg}} \left(\frac{Q_{\rm mg}}{Q_{\rm mp}}\right)^2 \frac{I_{\rm sg}}{I_{\rm sp}}, \qquad (2)$$

with $\phi^{\max}_{\rm sp}$ and $\phi^{\max}_{\rm sg}$ being the maximum voltage drops across each sheath (note that $\phi^{\max}_{\rm sp} < 0$ V and $\phi^{\max}_{\rm sg} > 0$ V). The variables on the right hand side of equation (2) correspond to the respective electrode surface areas $A_{\rm p}$ and $A_{\rm g}$, the respective mean charge densities in each sheath $\bar{n}_{\rm sp}$ and $\bar{n}_{\rm sg}$, the maximum uncompensated charges in each sheath $Q_{\rm mp}$ and $Q_{\rm mg}$, and the sheath integrals for each sheath $I_{\rm sp}$ and $I_{\rm sg}$ (for details see [17, 20, 58]). The symmetry parameter ε compares the plasma conditions at each sheath to determine the influence on the DC self-bias due to any spatial asymmetry (from different effective electrode surface areas), or from plasma sheath parameters, which affect the generation of a DC self-bias (η). The effect of the difference between the driving voltage waveform's global extrema on both the symmetry parameter and the DC self-bias can thus be referred to as the amplitude asymmetry effect (AAE). By using two or more consecutive harmonics of a fundamental frequency with distinct phases, $\left|\tilde{\phi}_{\max}\right|$ and $\left|\tilde{\phi}_{\min}\right|$ can be made unequal.

The slope asymmetry effect (SAE) is described in detail in the works of Bruneau *et al* [49–52]. Qualitatively, the SAE is the result of a temporal asymmetry in the positive (rise) and negative (fall) slopes of the applied voltage waveform. As the applied voltage waveform determines the (differing) voltage drops across each individual sheath, this leads to drastically different sheath dynamics, with a quickly expanding sheath at one electrode and a slowly expanding sheath at the opposing electrode. For electropositive discharges operated in the α-heating mode, the 'fast' expanding sheath accelerates electrons and (at high pressures) induces ionization locally near the given electrode, leading to a higher local ion density compared to the other electrode [49–52] and inducing an electrical asymmetry ($\varepsilon \neq 1$), as indicated by equation (2). The SAE may also affect other parameters associated with ε such as the sheath integrals [17, 20, 58].

The influence of the SAE on the electron power absorption and ionization dynamics will strongly depend on the electron heating mode, which in turn depends on pressure, driving frequency, and the relative phases between harmonics [25–34, 37–39, 41, 49–57, 59–61, 63–78]. In contrast to low pressure electropositive discharges (α-mode), a different heating mode caused by a significant electric field in the plasma bulk, known as the drift-ambipolar mode, has been observed in electronegative gases [40, 59, 61, 63, 66, 75, 79]. Under these conditions, electrons are accelerated towards the electrode during sheath collapse by a drift electric field in the plasma bulk and by ambipolar fields at the sheath edges. The drift electric field is a consequence of the reduced bulk conductivity, which itself is a result of the reduced electron density due to the attachment of electrons to the gas molecules, forming negative ions with low mobility. These negative ions are confined within the bulk plasma and do not generally reach the electrodes. The ambipolar field is the consequence of the peaked electron density at the sheath edges, which create strong density gradients towards the bulk [40, 59, 78]. Significant electron acceleration occurs in the bulk for this heating mode, and strong local field reversals which also cause electron energy gain can be observed at the collapsing sheath edge [68–70, 79, 80]. If this heating during sheath collapse (field reversal heating) is dominant, the SAE will cause the discharge symmetry to be reversed compared to discharges operated in the α-mode [52].

Previous fundamental studies on the effects of voltage waveform tailoring on the electron power absorption and excitation/ionization dynamics have been mostly restricted to electropositive argon discharges operated in the α-mode [25–32, 39, 53–57]. The fundamental knowledge of these dynamics is incomplete for process relevant electronegative and reactive gases (e.g. CF_4, which is often used in processing applications), where different electron heating modes are dominant. The effects of different gas chemistries on the electron power absorption dynamics and the generation of a DC self-bias in RF discharges driven by tailored voltage waveforms are inadequately understood.

Here, we present the first systematic experimental investigation of the electron power absorption dynamics and the EAE in CCPs driven by tailored voltage waveforms operated in CF_4, where the drift-ambipolar heating mode is prevalent. Experimental measurements of the DC self-bias and phase-resolved optical emission spectroscopy (PROES) are combined with particle-in-cell (PIC) simulations to obtain a complete understanding of the electron power absorption dynamics. We investigate the effects of the gas pressure, the harmonics' phases, and the number of harmonics under the conditions of both the amplitude and slope asymmetry effects.

We show that, due to the presence of the drift-ambipolar electron heating mode [40, 59, 61, 63, 66, 75, 79], the effect of VWT on the electron power absorption and excitation dynamics in CF_4 can differ significantly from those in electropositive discharges. Mode transitions are observed as a function of pressure and harmonics' phases. These transitions drastically affect the discharge symmetry and heating dynamics. For specific harmonic phases, it is found that the discharge can be split into a strongly electronegative half and an electropositive (or weakly electronegative) half. In the strongly electronegative half, a high negative-ion density occurs close to one electrode. This unique structure is caused by a comparatively long time of sheath collapse, a strong ionization source adjacent to the electrode, and the creation of a potential well. Electrons are confined in this well and efficiently generate negative ions locally via dissociative attachment. These dynamics are induced by particular shapes of the driving voltage waveform and are expected to provide unique advantages for a variety of applications.

This paper is structured in the following way: in section 2, the experimental setup and all diagnostic methods are introduced. The PIC/MCC code used in the numerical studies is briefly described in section 3. The presentation of the results in section 4 is divided into two parts. First, systematic phase variations using different numbers of driving frequencies, i.e. voltage waveform tailoring, are performed at different pressures. Waveforms with specific sets of phases between harmonics are then used to study either the AAE or a non-optimized SAE. Second, sawtooth waveforms are studied as one important waveform shape at different pressures. From these studies, the slope asymmetry effect is enhanced and isolated from the amplitude asymmetry effect, since the absolute values of the global extrema for sawtooth waveforms are identical. In both parts, the formation of a DC self-bias and the spatio-temporal excitation dynamics are analyzed and understood based on the experimental and computational results. Finally, conclusions are drawn in section 5.

2. Experimental setup

2.1. Reactor and diagnostics

The experimental setup is shown in figure 1. The capacitively coupled plasma is operated inside a modified gaseous electronics conference (GEC) reference cell by applying specific multi-frequency voltage waveforms to the powered (bottom) electrode while keeping the other (top) electrode and the chamber walls grounded. Up to three consecutive harmonics of the fundamental frequency $f = 13.56$ MHz are applied to the system. The harmonics' amplitudes and relative phases are tuned in order to realize the prescribed voltage waveforms.

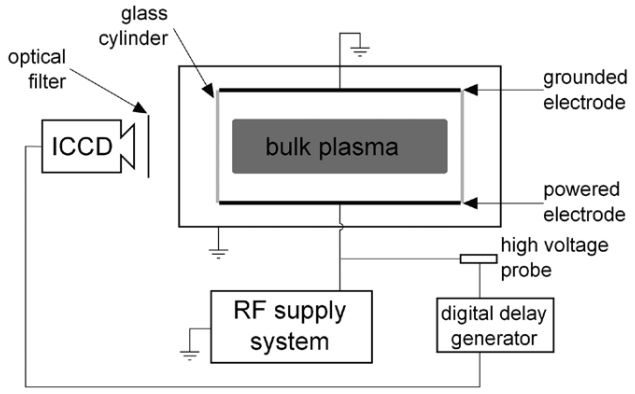

Figure 1. Sketch of the experimental setup consisting of a capacitively coupled GEC reference cell monitored by diagnostics (PROES via ICCD camera, and a high voltage probe for waveform monitoring/analysis).

A novel RF power supply system and impedance matching are used to generate these waveforms [47]. The system consists of three RF signal generators, each outputting a single frequency corresponding to one of the first three harmonics of the fundamental frequency, i.e. $f_1 = 13.56$ MHz, $f_2 = 27.12$ MHz, and $f_3 = 40.68$ MHz. These signals are phase-locked by a control unit and each generator's signal is matched individually before being combined at the powered electrode to drive the RF plasma. Electrical filters in each matching network prevent parasitic interactions between the signal branches [47].

The discharge is operated in CF_4 at pressures between 10 Pa and 100 Pa inside a 25 mm gap between two circular, stainless steel electrodes having a diameter of 10 cm. The plasma is radially confined between the electrodes by a glass cylinder. The discharge is slightly geometrically asymmetric due to capacitive coupling between the glass cylinder and the grounded side walls of the vacuum chamber [19, 81, 82]. This capacitive coupling effectively increases the grounded electrode area, which results in a small geometric asymmetry even though the material areas of each electrode are the same (see equation (2)) [81, 82]. Therefore, a negative DC self-bias is present even for single-frequency sinusoidal waveforms. At high pressures, the capacitive coupling between the cylinder and the walls has a weaker effect. The importance of the capacitive coupling between the cylinder and the grounded walls decreases because of the higher plasma density at high pressures, which increases the current flowing through the plasma and reduces the significance of the current flowing as a displacement current to the walls. The symmetry is significantly better at such higher pressures, and thus only the results at higher pressure will be compared with the results of the simulations, which assume perfect geometrical symmetry.

The plasma is investigated experimentally by utilizing two diagnostics: a high voltage probe and an ICCD (intensified charge-coupled device) camera used for PROES. The high voltage probe is attached to the coaxial cable connecting the combined frequency branches and the powered electrode (see figure 1) and allows measurements of the applied voltage waveform using an oscilloscope. The amplitudes and phases of the three consecutive harmonics of the voltage waveform are determined at the powered electrode's surface via Fourier analysis and a calibration routine previously used in dual- and triple-frequency discharges [19, 47]. This calibration procedure is performed by venting the chamber and attaching the high voltage probe to the powered electrode's surface. Comparisons of the voltage waveform parameters (harmonic amplitudes, phases) at the measurement point on the coaxial cable and at the electrode surface yield calibration factors for each harmonic's amplitude and phase. These calibration factors are strongly system dependent and are different for each applied frequency. This calibration procedure relies on the assumption that the impedance of the plasma is similar to the impedance when the chamber is vented, which is usually valid for CCPs due to their low plasma densities compared with inductively coupled plasmas or hybrid setups [19]. The high voltage probe and oscilloscope are used to tune the voltage waveform parameters as necessary to achieve the desired waveform.

In order to perform phase-resolved optical emission spectroscopy (PROES), an ICCD camera with an optical filter is placed outside a GEC cell viewport. PROES is a non-intrusive diagnostic that probes the dynamics of highly energetic electrons, which sustain the discharge through ionization, with high spatial and temporal resolutions within the RF period [66–68, 83–85]. Emission from a specifically chosen Flourine transition at 703.7 nm with a lifetime of about 26.3 ns [86] is resolved in space and time by this nanosecond-gated, high repetition rate ICCD camera (Andor iStar) synchronized with the applied RF voltage waveform. A more complete description of PROES can be found in [83]. Analysis of PROES data via a simple collisional-radiative model [83] yields the experimental spatio-temporal excitation rate plots. These plots have a spatial resolution better than 1 mm and a temporal resolution of about 2 ns.

2.2. Driving voltage waveforms

Different types of voltage waveforms are used to drive the CCP. The 'peaks'/'valleys' waveforms are applied to optimize the AAE (see figure 2(a)), while the sawtooth waveforms are used to optimize and study the SAE separately from the AAE (see figure 2(c)). Intermediate waveforms shown in figure 2(b) isolate the SAE from the AAE, but do not optimize the SAE. All waveforms are generated as a superposition of multiple consecutive harmonics [25–32, 39]:

$$\tilde{\phi}(t) = \sum_{k=1}^{N} \phi_k \cos(2\pi k f t + \theta_k), \tag{3}$$

where N is the total number of harmonics. k is the harmonic index, $f = 13.56$ MHz is the fundamental frequency, ϕ_k are the harmonics' amplitudes, and θ_k are the harmonics' phases. The total possible amplitude of the waveform is $\phi_{\text{tot}} = \sum_{k=1}^{N} \phi_k$, but because of destructive interference between the harmonics, this amplitude is not reached for every set of phases. The phase of the first harmonic (13.56 MHz), i.e. θ_1, is subtracted from all phases such that $\theta_1 = 0°$ for any waveform. Therefore, the other harmonics' phases (θ_k, $k \neq 1$) are relative to the phase of the fundamental 13.56 MHz component in equation (3).

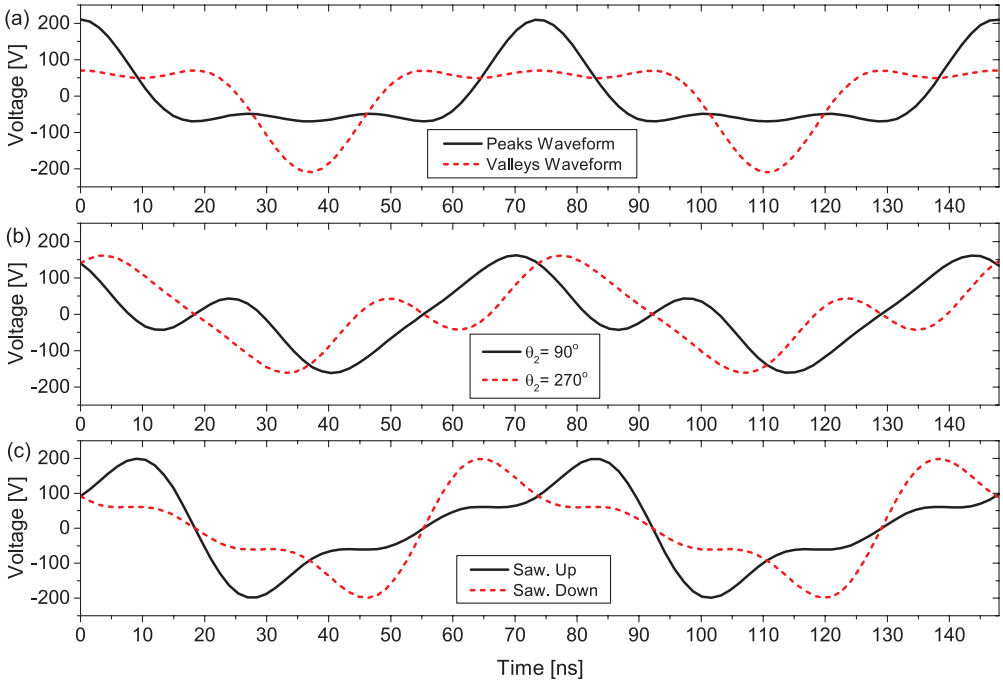

Figure 2. Examples of applied voltage waveforms over two consecutive RF periods for $N = 3$ harmonics: (a) 'Peaks' (solid) and 'Valleys' (dashed) waveforms (equations (3) and (4)), (b) intermediate waveforms where $\theta_2 = 90°$ (solid) and $\theta_2 = 270°$ (dashed) and all other phases are zero (equations (3) and (4)), and (c) sawtooth up (solid) and down (dashed) waveforms (equations (3) and (5)).

'Peaks' waveforms are generated by setting all phases to zero ($\theta_k = 0°$), while $\theta_2 = 180°$, $\theta_1 = \theta_3 = 0°$ define the 'Valleys' waveforms. The intermediate waveforms shown in figure 2(b) are generated by choosing $\theta_1 = \theta_3 = 0°$ and either $\theta_2 = 90°$ or $\theta_2 = 270°$. The harmonics' amplitudes are chosen according to the following criterion [25]:

$$\phi_k = \phi_{\text{tot}} \frac{2(N-k+1)}{N(N+1)}. \tag{4}$$

We set $\phi_{\text{tot}} = 210$ V. Dual- ($\phi_1 = 140$ V, $\phi_2 = 70$ V) and triple- ($\phi_1 = 105$ V, $\phi_2 = 70$ V, $\phi_3 = 35$ V) frequency cases are studied.

For sawtooth waveforms, the harmonic amplitudes are chosen according to the following criterion [49–52]:

$$\phi_k = \phi_N \frac{1}{k}, \tag{5}$$

where ϕ_N changes with the total number of harmonics (N). Here we study the triple-frequency case ($N = 3$) with $\phi_N = 138$ V and thus $\phi_1 = 138$ V, $\phi_2 = 69$ V, and $\phi_3 = 46$ V. The resulting waveform oscillates between the peak values ± 200 V. The total possible amplitude $\phi_{\text{tot}} = 253$ V was chosen so that the absolute possible positive and negative voltages were approximately the same as those reached by the AAE waveforms. For the sawtooth up waveform, the phases are set to $\theta_1 = 0°$, $\theta_2 = 270°$, and $\theta_3 = 180°$. The sawtooth down waveform has phases $\theta_1 = 0°$, $\theta_2 = 90°$, and $\theta_3 = 180°$. This choice of individual harmonic amplitudes and phases makes the slope of the slowly rising/falling part of the waveform more linear and the fast drop/rise steeper (see figure 2(c)), thus enhancing the SAE.

Historically, waveforms designed from the harmonics' amplitudes criterion of equation (4) were used before the use of sawtooth waveforms and will therefore be called 'classical tailored voltage waveforms' in this work.

3. Simulations

Our numerical studies of CF_4 plasmas are based on a bounded 1D3V particle-in-cell simulation code, complemented with a Monte Carlo treatment of collision processes (PIC/MCC) [87–89]. The electrodes are assumed to be planar and parallel. To further simplify, the large aspect ratio (electrode diameter over electrode separation) of the experimental device justifies neglecting the radial losses. The discharge modeled by the code is assumed to be perfectly geometrically symmetric. The powered electrode is driven by the voltage waveforms specified in section 2.2, while the other electrode is grounded.

The charged species taken into account in the model are CF_3^+, CF_3^-, F^-ions, and electrons. The cross-sections of electron-CF_4 collision processes (see table 1) are adopted from Kurihara *et al* [90], with the exception of electron attachment processes (producing CF_3^- and F^- ions), which are adopted from Bonham [91]. The electron-impact collision processes considered in the model are listed in table 1 and their energy dependent cross-sections are displayed in figure 3. As a simplification, the processes that create radicals, or charged species other than CF_3^+, CF_3^-, and F^-, are allowed to affect only the electron kinetics and the products are not otherwise accounted for.

Ion-molecule reactive reactions, as well as elastic collisions are also considered in the simulation [92–95]. For the elastic collisions of ions with buffer gas molecules, we adopt Langevin type cross-sections:

Table 1. List of electron-CF_4 molecule collision processes considered in the model.

Collision partners	Description	Product	E_0
$e^- + CF_4$	Elastic momentum transfer		0
$e^- + CF_4$	Vibrational excitation		0.108
$e^- + CF_4$	Vibrational excitation		0.168
$e^- + CF_4$	Vibrational excitation		0.077
$e^- + CF_4$	Electronic excitation	CF_4^*	7.54
$e^- + CF_4$	Dissociative ionization	$CF_3^{+\,+}$	41
$e^- + CF_4$	Dissociative ionization	CF_3^+	16
$e^- + CF_4$	Dissociative ionization	$CF_2^{+\,+}$	42
$e^- + CF_4$	Dissociative ionization	CF_2^+	21
$e^- + CF_4$	Dissociative ionization	CF^+	26
$e^- + CF_4$	Dissociative ionization	C^+	34
$e^- + CF_4$	Dissociative ionization	F^+	34
$e^- + CF_4$	Attachment	F^-	0
$e^- + CF_4$	Attachment	CF_3^-	0
$e^- + CF_4$	Neutral dissociation	CF_3	12
$e^- + CF_4$	Neutral dissociation	CF_2	17
$e^- + CF_4$	Neutral dissociation	CF	18

Note: E_0 is the threshold energy in eV [90, 91].

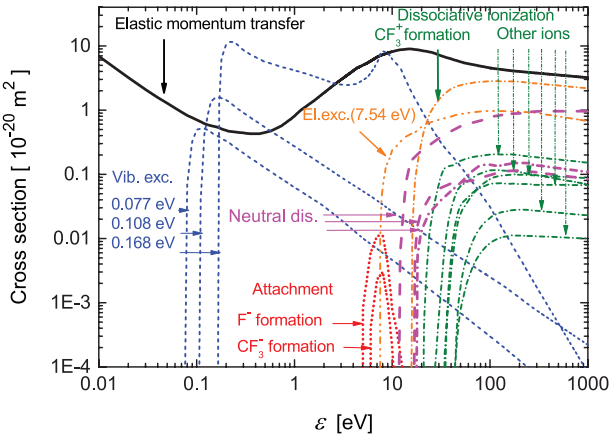

Figure 3. Cross-sections of electron-impact collision processes [90, 91].

$$\sigma_L = \left(\frac{\pi\alpha_p e^2}{\epsilon_0 \mu}\right)^{1/2} \beta_\infty^2 g^{-1}, \tag{6}$$

where μ is the reduced mass, α_p is the polarizability, g is the relative velocity of the colliding partners, and β_∞ is the dimensionless impact parameter for which the deflection angle is negligible [92–94]. The ion-molecule reaction processes considered in our model are listed in table 2 and their cross-sections are shown in figure 4.

The ion-molecule reactions produce the charged species considered in the model (CF_3^+, CF_3^-, F^-, and e^-), with the exception of the first reaction in table 2 that results in the formation of CF_2^+ ions. CF_2^+ and CF_3^+ ions react similarly with CF_4 and the recombination rate of CF_2^+ with electrons is only

Table 2. Ion-CF_4 molecule collision processes considered in the model.

Projectile	Reaction	E_0
CF_3^+	$CF_3^+ + CF_4 \rightarrow CF_2^+ + CF_4 + F$	5.843
CF_3^+	$CF_3^+ + CF_4 \rightarrow CF_3^+ + CF_3 + F$	5.621
CF_3^+	$CF_3^+ + CF_4 \rightarrow CF_3^+ + CF_4$	0
CF_3^-	$CF_3^- + CF_4 \rightarrow CF_4 + CF_3 + e^-$	1.871
CF_3^-	$CF_3^- + CF_4 \rightarrow CF_3^- + CF_3 + F$	5.621
CF_3^-	$CF_- + CF_4 \rightarrow CF_2 + CF_4 + F^-$	1.927
CF_3^-	$CF_3^- + CF_4 \rightarrow CF_3^- + CF_4$	0
F^-	$F^- + CF_4 \rightarrow CF_4 + F + e^-$	3.521
F^-	$F^- + CF_4 \rightarrow CF_3 + F^- + F$	5.621
F^-	$F^- + CF_4 \rightarrow F^- + CF_4$	0

Note: E_0 is the threshold energy in eV [92–95].

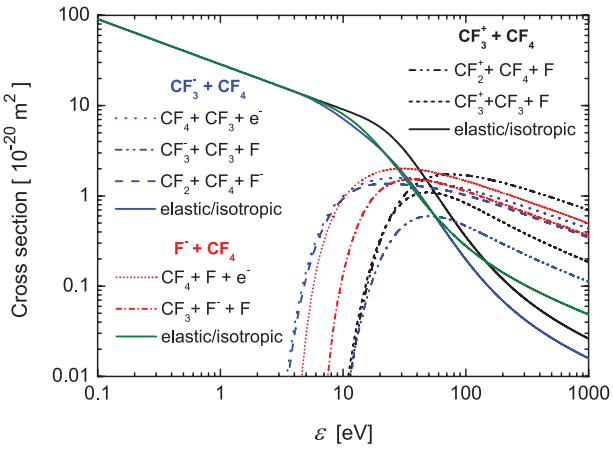

Figure 4. Cross-sections of ion-impact collision processes [92–95].

Table 3. Recombination processes considered in the model.

Reaction	Rate coefficient ($m^3\ s^{-1}$)
$CF_3^+ + e^-$	$3.95 \times 10^{-15} T_i^{-1} T_e^{-0.5}$
$CF_3^+ + F^-$	5.5×10^{-13}
$CF_3^+ + CF_3^-$	5.5×10^{-13}

Note: The ion and electron temperatures, T_i and T_e, respectively, are given in electronvolts [91, 98–100].

slighter higher than the recombination rate of CF_3^+ [96]. We assume, as a simplification, that the above CF_2^+ generation process does not convert CF_3^+ ions to CF_2^+ ions. This is further justified by the high rates for CF^+-neutral and CF_2^+-neutral reactions, which convert these lighter ions into CF_3^+ ions [97]. This assumption makes it unnecessary to introduce an additional type of charged species of minor importance into the computations and improves the balance of positive ion density.

Recombination processes between positive and negative ions as well as between electrons and CF_3^+ ions are simulated according to the procedure outlined in the work of Nanbu and Denpoh [98]. The ion–ion recombination rate coefficients are

adopted from Proshina *et al* [99], while the rate for the electron-CF_3^+ recombination process is from Denpoh and Nanbu [100]. The recombination processes are listed in table 3.

In the simulations, we assume a gas temperature of 350 K. We include the emission of secondary electrons from the electrodes due to ion impact via the secondary electron emission coefficient, γ, which is set at $\gamma = 0.4$ for the best agreement with experimental results. In the experiment, the plasma is reactive and operates at a relatively high pressure. Consequently, a thin film with unknown properties is deposited on the electrode. This high secondary electron emission coefficient in the simulations is required to reproduce the experimentally measured DC self-bias. The excitation rate from energetic secondary electrons is smaller in CF_4 compared to Argon due to the lower positive ion flux in CF_4. The secondary electrons also cause more ionization than excitation due to their differing cross sections and can strongly affect the discharge symmetry via ionization in the sheaths. The (elastic) reflection of electrons from the electrodes is also considered; we adopt a reflection probability value of 0.2 [101].

For the specific driving voltage waveforms used here, a DC self-bias generally builds up on the powered electrode (which is capacitively coupled) in order to equalize the time-averaged electron and positive ion fluxes to each of the electrodes. Negative ions are confined within the bulk and do not reach the electrodes. This self-bias is adjusted in the simulation in an iterative way to satisfy the current (i.e. flux) balance requirement mentioned above.

The electron-impact excitation rate from ground-state F atoms to the excited F-level responsible for the 703.7 nm emission observed experimentally by PROES is approximated in the simulation using the cross-section for the electronic excitation process for CF_4 having a threshold of 7.54 eV (see figure 3 and table 1) by specifically accumulating excitation data for electrons with energies equal to or higher than 14.5 eV. This calculation is used exclusively for diagnostic purposes and does not affect the total electronic excitation calculated in the code. We further assume that the F atom density is uniform in space and does not vary over time. In this way, we compare the simulated spatio-temporal dynamics of electrons to the experimental PROES measurements without explicitly including F atoms in the simulation.

4. Results

This section is divided into two parts according to the different shapes of the driving voltage waveform used to operate the CCP. First, classical tailored voltage waveforms are used based on harmonics' amplitudes chosen according to equation (4) and a systematic variation of θ_2 ($\theta_1 = \theta_3 = 0°$). Such waveforms generate a pure AAE ('Peaks'/'Valleys' waveforms), or a non-optimized SAE ($\theta_2 = 90°, 270°$ waveforms). Second, sawtooth waveforms are used to isolate the SAE from the AAE, while also optimizing the SAE. The harmonics' amplitudes are chosen according to equation (5) with $\theta_1 = 0°$, $\theta_2 = 270°$, $\theta_3 = 180°$ for sawtooth up waveforms and $\theta_1 = 0°$, $\theta_2 = 90°$, $\theta_3 = 180°$ for sawtooth down waveforms.

The effects of each voltage waveform on the spatio-temporal electron power absorption dynamics and the generation of a DC self-bias are studied by a synergistic combination of experiments and simulations to obtain a complete interpretation of the effect of using a reactive electronegative gas such as CF_4 on the EAE in CCPs driven by customized voltage waveforms.

4.1. Amplitude asymmetry

A driving voltage waveform according to equation (3), with amplitudes according to equation (4), is used. Single- ($N = 1$), dual- ($N = 2$), and triple- ($N = 3$) frequency scenarios are investigated. Here, $\phi_{tot} = 210$ V is kept constant while θ_2 is varied. Two different pressures of 20 Pa and 80 Pa are used to study a weakly electronegative (20 Pa) and a strongly electronegative (80 Pa) scenario.

The measured and simulated DC self-bias voltages are shown in figure 5 as a function of the second harmonic's phase (the 27 MHz signal's phase, θ_2) for both 80 Pa and 20 Pa. The other harmonics' phases are fixed at zero throughout these variations. In the experiment, the discharge is always geometrically asymmetric at 20 Pa, as indicated by the $\eta \approx -29$ V value obtained for $N = 1$ (see figure 5(a)). Therefore, we do not compare the 20 Pa measurements to the results of the (geometrically symmetric) simulation. At 20 Pa, the control range of η is increased by using more harmonics for the same total voltage, due to an enhanced amplitude asymmetry effect (AAE) similar to the AAE in electropositive argon discharges [19–24, 31, 32, 39]. For 80 Pa, the control range of η is larger for $N = 2$ compared to $N = 3$ and the functional dependence of the bias on the phase is significantly different. This is caused by the presence of a different electron heating mode which enhances the slope asymmetry effect (SAE) for $N = 2$ at phases around 90° and 270°. This heating mode will be discussed later in this section. The $N = 2$ DC self-bias caused by the SAE at $\theta_2 = 90°$ is almost the same as the one caused by the AAE at $\theta_2 = 180°$. Such an effect is not observed in the $N = 3$ case.

Figure 6 shows spatio-temporal plots of the different plasma parameters obtained from the experiment and the simulation, for $\theta_2 = 0°$ and $N = 3$. Figures 6(a) and (b) show the spatio-temporal excitation rate and the electric field obtained from the simulation at 80 Pa, while figures 6(c) and (d) show the excitation rate obtained experimentally at 80 Pa and 20 Pa, respectively. In the experiment, the excitation at the (bottom) powered electrode is enhanced with respect to the maxima observed at the grounded electrode due to the geometric asymmetry of the reactor. This does not happen in the simulation and, therefore, the excitation rate at the powered electrode is stronger in the experiment compared to the simulation. Nevertheless, good qualitative agreement is found throughout. The asymmetry of the discharge drastically changes between 20 and 80 Pa as the excitation maximum near the powered electrode moves towards the grounded electrode at higher pressures as the result of a heating mode transition. At 20 Pa, α-mode heating is dominant (see figure 6(d)), whereas drift-ambipolar mode heating is prevalent at 80 Pa (see figures 6(a)

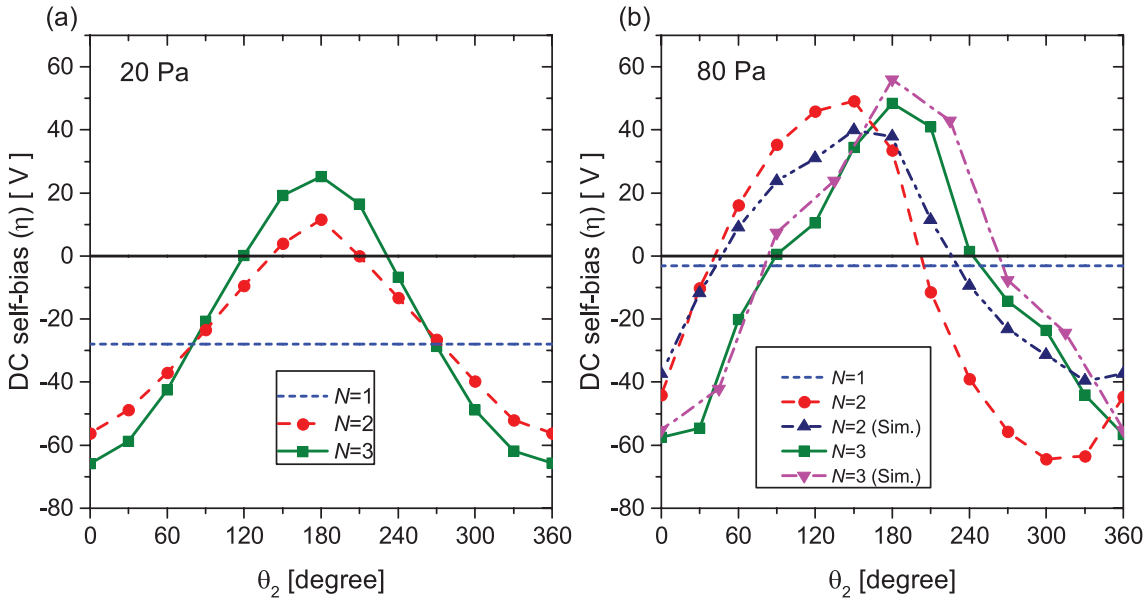

Figure 5. DC self-bias as a function of θ_2 for (a) 20 Pa (experimentally measured bias) and (b) 80 Pa (including both the experimentally measured bias and the bias obtained from the PIC simulation, a.k.a. 'Sim.') for different numbers of applied harmonics, $N = 1, 2, 3$. $\phi_{tot} = 210$ V for all cases.

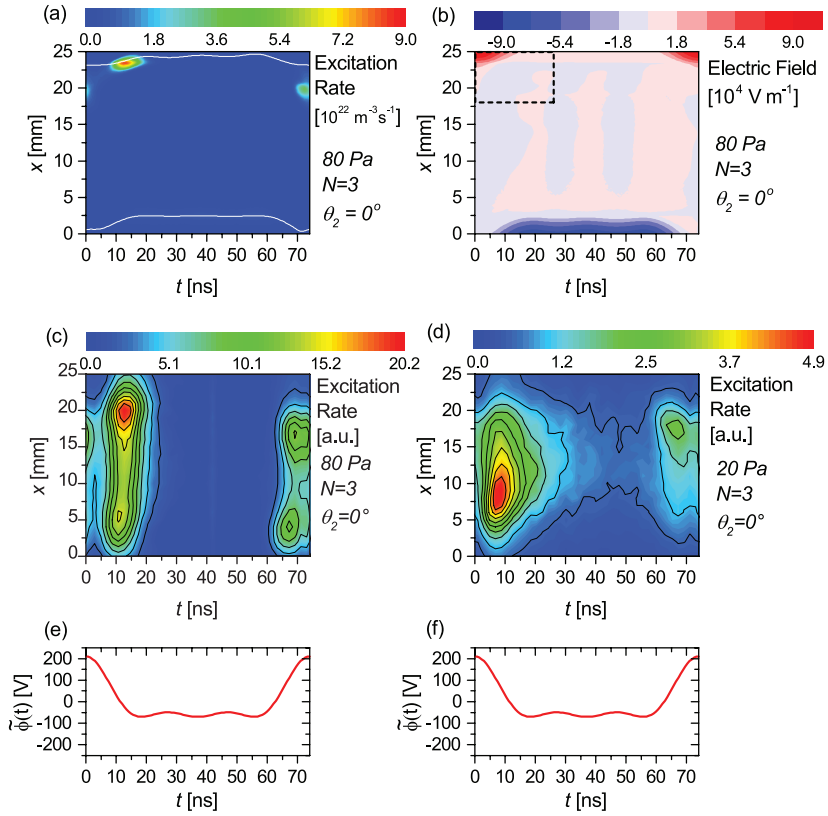

Figure 6. Spatio-temporal plots for $N = 3$, $\theta_2 = 0°$ ('Peaks' waveform) of (a) the excitation rate at 80 Pa obtained from the PIC simulation with the sheath edges shown in white, (b) the electric field at 80 Pa obtained from the simulation, (c) the experimentally measured excitation rate at 80 Pa, and (d) the experimentally measured excitation rate at 20 Pa. The applied voltage waveform is shown in (e) and (f) for reference, for $\phi_{tot} = 210$ V. The dashed region in (b) designates the region of high bulk electric field shown in figure 7(a). The powered electrode is situated at $x = 0$, while the grounded electrode is located at $x = 25$ mm.

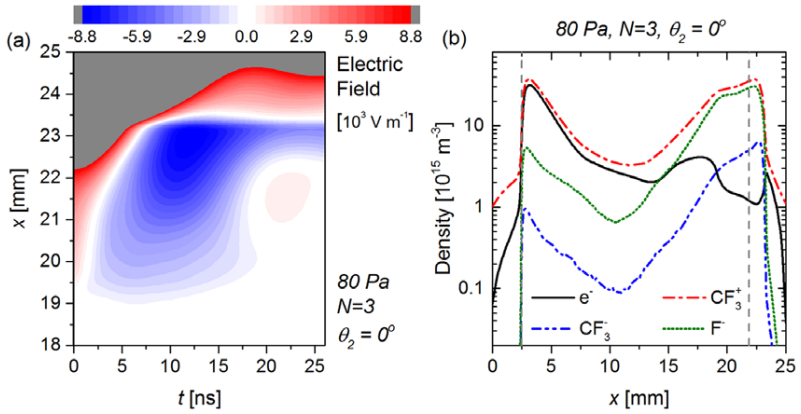

Figure 7. (a) Spatio-temporal plot of the electric field at the beginning of one fundamental RF period close to the grounded electrode for 80 Pa, $\theta_2 = 0°$ ('Peaks' waveform, $N = 3$, $\phi_{tot} = 210$ V) obtained from the simulation, zoomed into the region of interest in figure 6(b). Time-averaged density profiles from the PIC simulations for all charged species. The dashed lines indicate the maximum sheath widths of the powered sheath (2.48 mm) and grounded sheath (3.13 mm).

and (c)). This transition is caused by the low electronegativity (and collisionality) at 20 Pa and the high electronegativity (and higher collisionality) in combination with specific electron dynamics at 80 Pa. At this high pressure a strong excitation maximum is observed at the collapsing sheath edge close to the grounded electrode (see figure 6(a)), which originates from a strong drift and an ambipolar electric field caused by the high local electronegativity [40, 59, 61, 63, 66, 75, 79]. The high local electronegativity is caused by a unique mechanism induced by the shape of the driving voltage waveform, which causes the sheath at the grounded electrode to be collapsed for most of the fundamental RF period. This does not happen at the powered electrode. Therefore, at the grounded electrode, negative ions can enter the sheath region, since the time-averaged electric field is very small and only weakly repels these ions from this region. Consequently, the local electron density and conductivity are depleted and a strong reversed electric field is generated by the high RF current which occurs during the sheath collapse [69]. This electric field causes an excitation maximum at the grounded electrode which is further analyzed in figure 7.

Figure 7(a) shows the reversed electric field and the presence of a potential well formed near the grounded electrode by the (floating) sheath electric field at the electrode during its sheath collapse and an ambipolar field at the bulk plasma side caused by the local slope of the electron density profile (see figure 7(b)) [59]. This peak in the electron density near the grounded sheath edge is generated near the time of sheath collapse (around 12–17 ns) and decays slowly throughout the RF period, as there is no sheath expansion to repel these electrons (until around 65 ns). The peak in electron density and, by extension, the ambipolar electric field, persists throughout the RF period and appears prominently in the time-averaged electron density shown in figure 7(b). Electrons are accelerated by the reversed electric field and are confined in this potential well. Depending on the energy of the electrons accelerated by the field reversal and those confined in this well, ionization (e.g. CF_3^+ generation) or attachment (CF_3^- and F^- generation) proceeds very efficiently, as shown in the marked regions of figure 8. Low energy electrons attach to CF_4 molecules more efficiently compared to high energy electrons, due to the differences in the cross-sections (see figure 3). This mechanism leads to strong ionization and a source of negative ions inside the sheath region at the grounded electrode. In this way, an even stronger field reversal is generated due to a further local depletion of the conductivity. These effects are self-amplifying until the plasma stabilizes, making the effect self-sustaining (i.e. a closed loop). Consequently, this geometrically symmetric CCP becomes split into an electropositive (or weakly electronegative) half and a strongly electronegative half, due to the above mechanisms (see figure 7(b)).

Figure 8(a) also shows the presence of secondary electrons, which are accelerated in the sheath regions. However, they do not affect the ionization and attachment rates considerably (see figures 8(c) and (d)). Their contribution to the excitation also appears to be negligible in comparison to other power-coupling mechanisms (see figure 6).

The spatio-temporal excitation and electric field plots at $\theta_2 = 180°$ (see figure 9) mirror those at $\theta_2 = 0°$. The simulated excitation and electric field are exact mirrors of the $\theta_2 = 0°$ simulation results, as there is no geometric asymmetry there. The experimental PROES plots are affected by the geometric asymmetry in the experiment, but still closely mirror one another. Here, the region close to the powered electrode is electronegative, while the region close to the grounded electrode is electropositive (i.e. weakly electronegative), according to the simulation. An intermediate regime is found at $\theta_2 = 90°$ (see figure 10), where the applied waveform utilizes a non-optimized slope asymmetry effect.

Several heating mode transitions can be observed as a function of θ_2 or pressure. Specifically, a clear transition from the α-heating mode to the drift-ambipolar mode occurs between 20 and 80 Pa for fixed harmonics' phases and voltage amplitudes (see figures 6, 9 and 10), with the drift-ambipolar mode being favored at higher pressures due to the higher electronegativity and higher collisionality at higher pressures.

Figure 11 demonstrates that adding higher harmonics enhances the sheath expansion heating relative to the

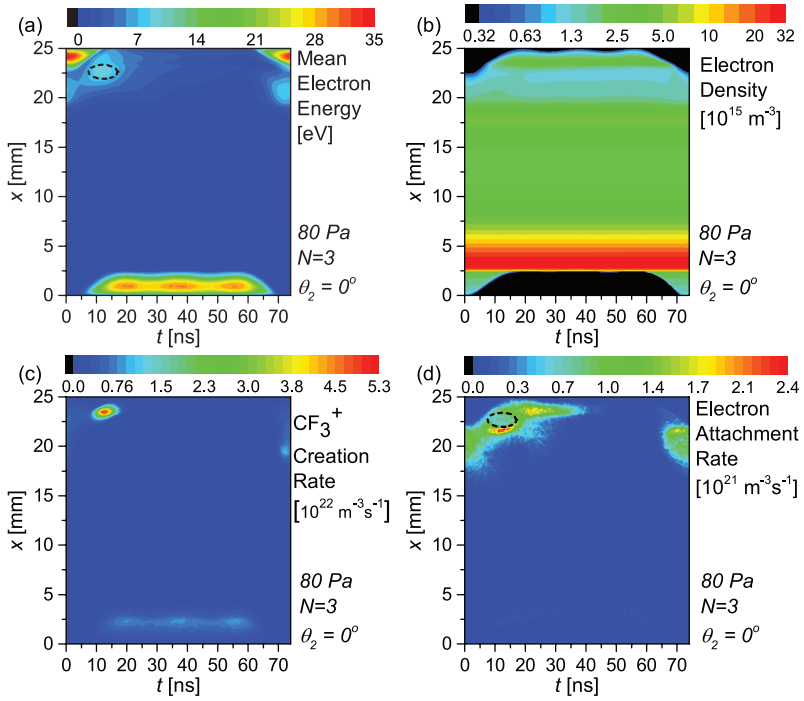

Figure 8. Spatio-temporal plots for 80 Pa, $\theta_2 = 0°$ ('Peaks' waveform, $N = 3$, $\phi_{tot} = 210$ V) of (a) mean electron energy, (b) electron density, (c) rate of CF_3^+ creation, and (d) rate of electron attachment (i.e. CF_3^- and F^- creation), as obtained from the simulation.

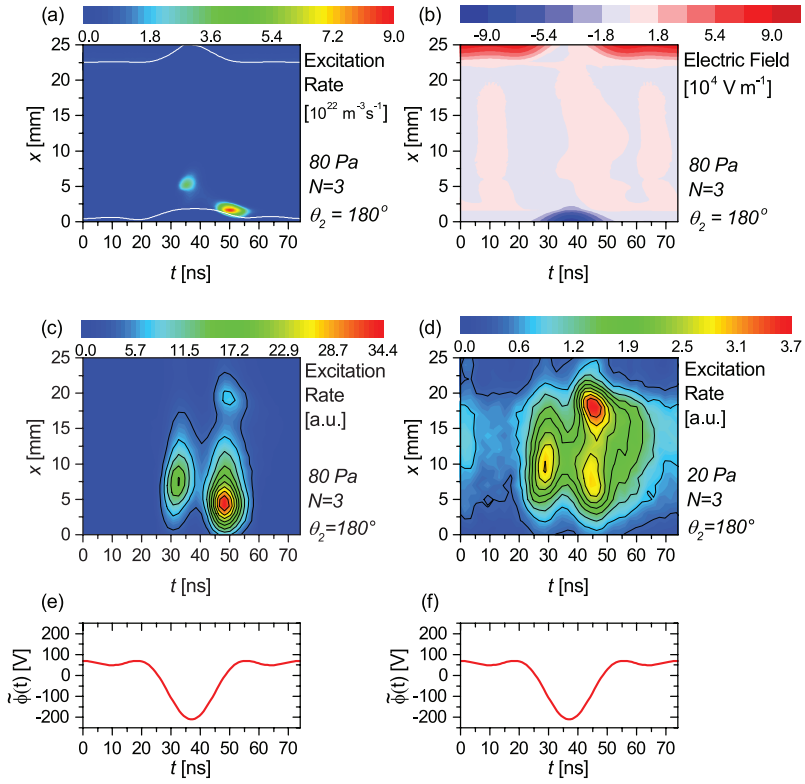

Figure 9. Spatio-temporal plots for $\theta_2 = 180°$ ('Valleys' waveform, $N = 3$, $\phi_{tot} = 210$ V) of (a) the excitation rate at 80 Pa obtained from the simulation with the sheath edges shown in white, (b) the electric field at 80 Pa obtained from the simulation, (c) the experimentally measured excitation rate at 80 Pa, and (d) the experimentally measured excitation rate at 20 Pa. The applied voltage waveform is shown in (e) and (f) for reference.

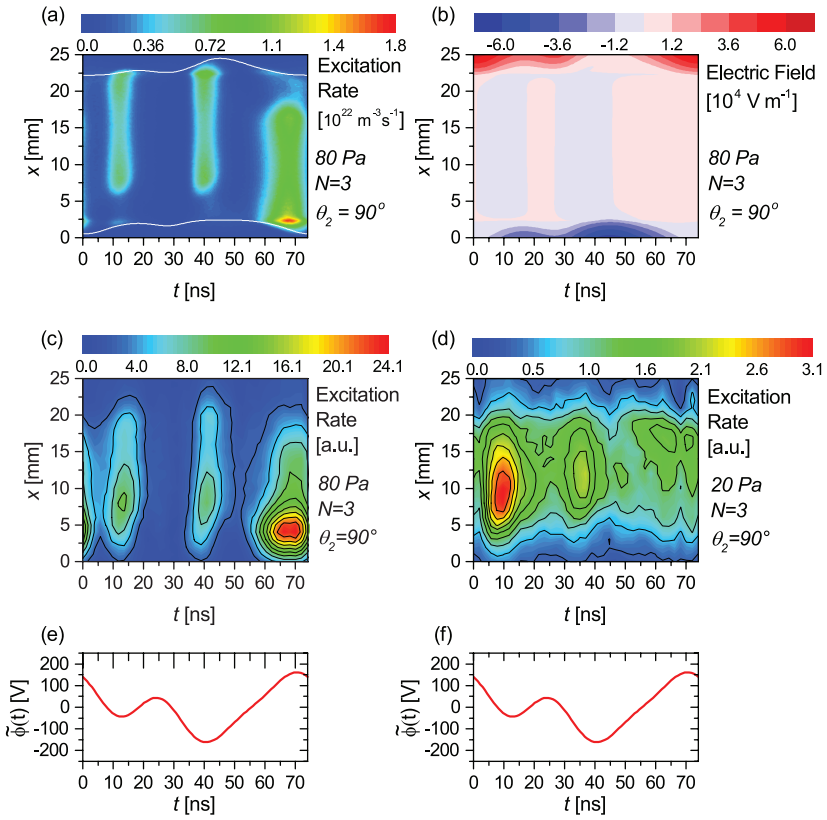

Figure 10. Spatio-temporal plots for $\theta_2 = 90°$ ($N = 3$, $\phi_{tot} = 210$ V) of (a) the excitation rate at 80 Pa obtained from the simulation with the sheath edges shown in white, (b) the electric field at 80 Pa obtained from the simulation, (c) the experimentally measured excitation rate at 80 Pa, and (d) the experimentally measured excitation rate at 20 Pa. The applied voltage waveform is shown in (e) and (f) for reference.

drift-ambipolar heating. This is due to an increase of the driving waveform's slope during sheath expansion, which increases the effectiveness of α-mode heating. For $\theta_2 = 270°$, this leads to more spatially symmetric excitation dynamics for $N = 3$, since the sheath expansion heating at the powered electrode is enhanced relative to the heating at the grounded electrode at about 28 ns. In terms of the symmetry parameter from equation (2), ε is less than unity for $N = 2$ and ε is approximately unity for $N = 3$ at $\theta_2 = 270°$. Thus, we find a negative DC self-bias for two harmonics at $\theta_2 = 270°$, and almost no bias at the same phase for $N = 3$ (see figure 5). The strongly negative bias for $N = 2$ at this phase is caused by the SAE, although its effect is reversed compared to electropositive gases due to the presence of the drift-ambipolar heating mode. In electropositive gases such as argon, positive DC self-biases are often observed for this phase [49–52].

4.2. Slope asymmetry

The sawtooth waveforms used here (see figure 2(c)) are realized with the fixed phases and amplitudes defined in section 2; these waveforms consist of three consecutive harmonics of $f = 13.56$ MHz, each with an amplitude according to equation (5). The amplitudes and phases of the sawtooth up waveform for $N = 3$ are: $\phi_1 = 138$ V, $\phi_2 = 69$ V, $\phi_3 = 46$ V, $\theta_1 = 0°$, $\theta_2 = 270°$, and $\theta_3 = 180°$. The sawtooth up waveform yields a fast sheath expansion at the powered electrode as a result of the fast transition from its maximum positive applied voltage to its maximum negative applied voltage, and a fast sheath contraction at the grounded electrode. Conversely, the sawtooth down waveform yields a fast expansion of the grounded sheath as the fast transition occurs from the maximum negative voltage to the maximum positive voltage. The $N = 3$ sawtooth down waveform has the same amplitudes and phases as listed above, with the exception that $\theta_2 = 90°$.

The experimentally obtained DC self-bias (η) for the sawtooth waveforms is plotted as a function of pressure in figure 12. A significant geometric asymmetry is present, especially at lower pressures ($p \leqslant 30$ Pa), which prevents comparison of our experimental results to those of the PIC simulations. The bias changes drastically as a function of pressure as a result of the SAE and the geometric asymmetry of the discharge. No AAE can be present due to the identical global extrema in the driving voltage waveform. For the sawtooth down waveform, the sign of the self-bias changes as the pressure increases. In a geometrically symmetric reactor, this would also happen for the sawtooth up waveform. This reversal of the discharge asymmetry as a function of pressure is caused by a transition from the α-heating mode to the drift-ambipolar heating mode induced by increasing the pressure

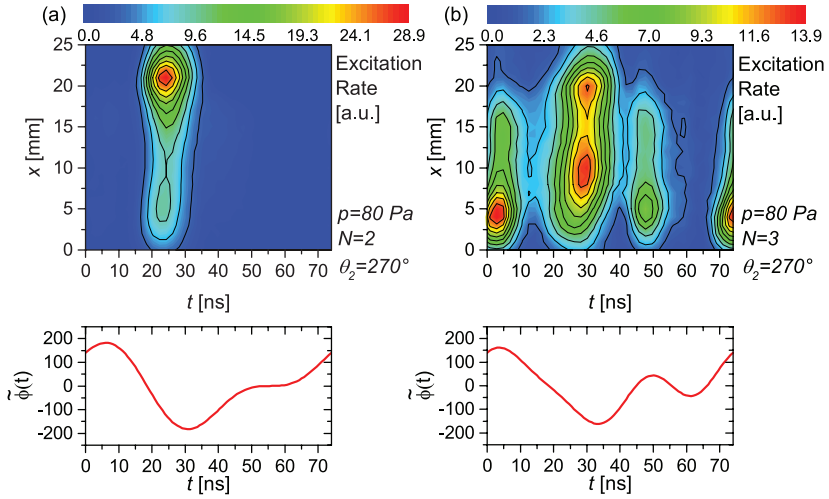

Figure 11. Spatio-temporal plots for $\theta_2 = 270°$ ($\phi_{tot} = 210$ V) at 80 Pa of (a) the experimentally measured excitation rate for $N = 2$ and (b) the experimentally measured excitation rate for $N = 3$. The applied voltage waveforms are shown below the spatio-temporal plots for reference.

and thus increasing the electronegativity. Above 50 Pa, the self-bias stays approximately constant as a function of pressure after this mode transition. This is expected to be highly relevant for applications, as it completely reverses the role of the two electrodes with regards to the EAE. For example, a negative DC self-bias voltage corresponds to enhanced excitation at the grounded side, whereas, in electropositive plasmas, it corresponds to enhanced excitation at the powered side.

The sawtooth down waveform causes the grounded sheath to expand quickly and the sheath at the powered electrode to expand slowly, while for the sawtooth up waveform the situation is reversed. At 20 Pa, the discharge operates in the α-heating mode (see figures 13(a) and (b)). At this low pressure, the discharge is geometrically asymmetric. This results in an increase of the excitation rate at the powered electrode relative to that at the grounded electrode. For the sawtooth down waveform, the spatio-temporal excitation rate at the grounded side during the grounded sheath expansion is more visible compared to that measured for a sawtooth up waveform, as the grounded sheath expands very quickly once per fundamental RF period. Due to the geometric asymmetry of the reactor, the density in the powered sheath is still higher than that in the grounded sheath, i.e. $\bar{n}_{sp} > \bar{n}_{sg}$. Thus, according to equation (2), the symmetry parameter ε is relatively high for this situation, though it is still less than unity due to the geometric asymmetry. The self-bias is then weakly negative at low pressures, according to equation (1).

At higher pressures (50 Pa and 80 Pa, see figures 13(c) and (d) and figures (e)–(f), respectively), the discharge operates in the drift-ambipolar heating mode and there is strong excitation at the powered/grounded electrode for the sawtooth up/down waveform, respectively, where the sheath collapses

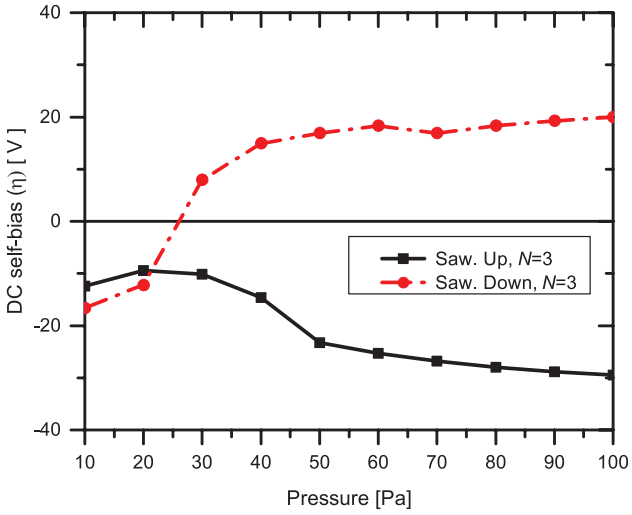

Figure 12. Experimentally measured DC self-bias voltage as a function of pressure for the sawtooth waveforms at $N = 3$ and $\phi_{tot} = 253$ V.

quickly once per fundamental RF period. This is caused by a mechanism similar to that described in section 4.1. The high negative-ion density leads to a local depletion of the electron density and a strong electric-field reversal at the edge of the rapidly collapsing sheath. The self-amplifying mechanism described before is only effective at one electrode for sawtooth waveforms, where electrons are accelerated towards the electrode (i.e. towards the potential well) and not away from it (and its corresponding sheath). In combination with a reactor with better geometric symmetry, this leads to $\bar{n}_{sp} \gg \bar{n}_{sg}$ for the sawtooth down waveform, where $\varepsilon > 1$ and a positive bias is generated, and $\bar{n}_{sp} < \bar{n}_{sg}$ for the sawtooth up waveform, where $\varepsilon < 1$ and a negative bias is generated. In conclusion, the

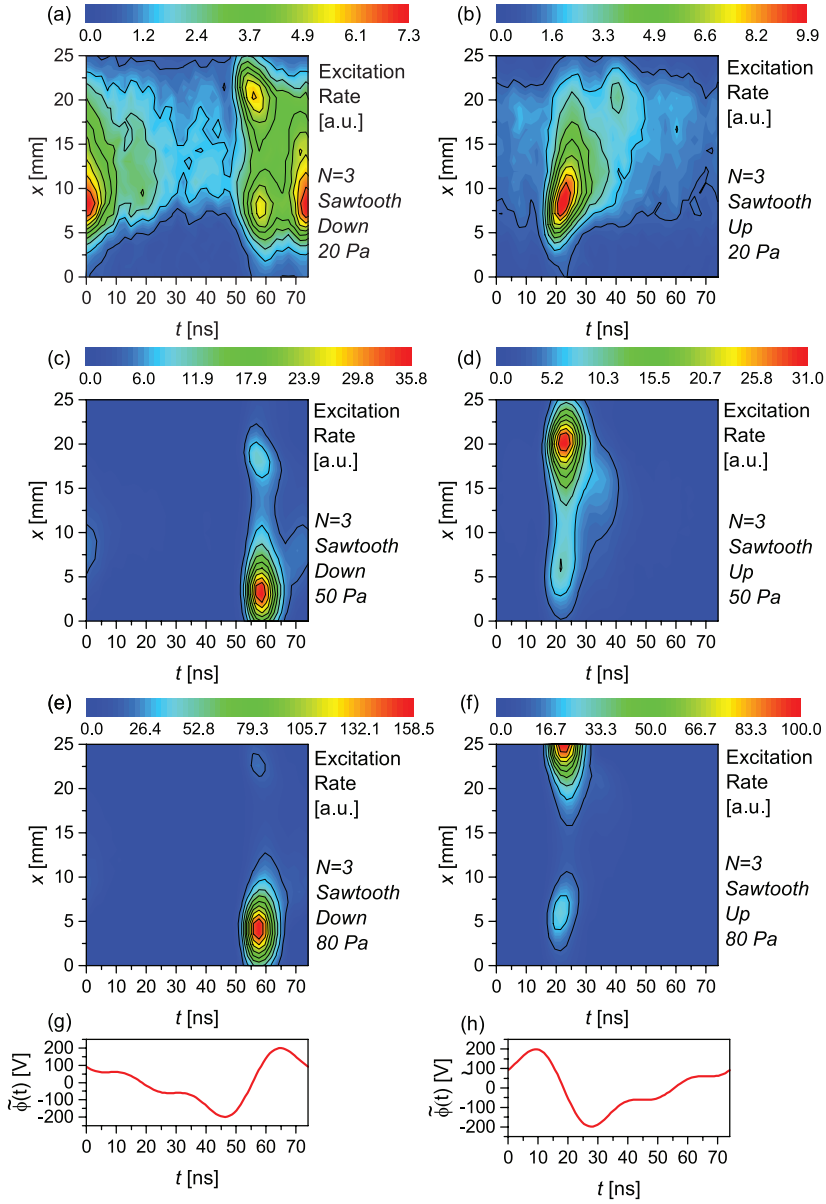

Figure 13. Experimentally measured spatio-temporal excitation rate for sawtooth waveforms ($N = 3$, $\phi_{tot} = 253$ V) at ((a)–(b)) 20 Pa, ((c)–(d)) 50 Pa, and ((e)–(f)) 80 Pa. The left column contains the sawtooth down ($\theta_2 = 90°$, $\theta_3 = 180°$) results, while the right column shows the sawtooth up ($\theta_2 = 270°$, $\theta_3 = 180°$) results. The applied voltage waveforms are shown in (g) and (h) for reference.

change of the DC self-bias and the reversal of the discharge symmetry as a function of pressure for the sawtooth waveforms can be explained by a transition to an electron heating mode characteristic of an electronegative plasma, which is induced by increasing the pressure.

5. Conclusions

The electron power absorption and excitation dynamics in capacitive CF_4 discharges driven by tailored voltage waveforms were investigated experimentally and via numerical simulations, with good qualitative agreement between the two. The discharge pressure, the number of harmonics, and the harmonics' phases were varied systematically. At high pressures the discharge was found to operate in the drift-ambipolar heating mode, while at low pressures the α-heating mode was dominant. Mode transitions between these two modes were induced by changing the pressure, the harmonics' phases, and the total number of harmonics.

The presence of the drift-ambipolar mode was found to lead to unique spatio-temporal excitation/ionization dynamics. Depending on the choice of the harmonics' phases, i.e. the shape of the applied voltage waveform, one strong excitation/ionization maximum per fundamental RF period can be generated at the collapsing sheath edge adjacent to only one electrode. This is due to the extended period where the sheath is

fully collapsed at this electrode in combination with a strong electric-field reversal that accelerates negatively charged particles towards this electrode. Therefore, negative ions can move into this sheath region and locally deplete the electron density and conductivity. This enhances the electric-field reversal at times of high RF current. Moreover, a potential well is formed at this electrode during sheath collapse by the electric field of the (floating) collapsed sheath and the ambipolar electric field in the bulk plasma. Electrons are accelerated by the reversed field toward this well and are confined efficiently in it, leading to an increase in the local attachment rate and the formation of negative ions leading to an increased negative-ion density in the sheath region only at one electrode. This depletes the local conductivity further, increasing the field reversal strength. These mechanisms lead to a self-amplification of the field reversal. In this way, the discharge becomes divided into an electropositive half at one electrode and an electronegative half at the other electrode.

The generation of a DC self-bias via the EAE was found to be strongly affected by the electron heating mode. This was particularly true for sawtooth waveforms, where only the slope asymmetry effect (SAE) causes an electrical generation of a DC self-bias. For such waveforms, the sign of the DC self-bias can be reversed by switching from the α-heating mode to the drift-ambipolar heating mode by increasing the pressure due to strongly different excitation/ionization dynamics. Thus, the discharge asymmetry is reversed in electronegative CF_4 plasmas operated by sawtooth waveforms in the drift-ambipolar heating mode compared to electropositive plasmas operated in the α-heating mode (e.g. CF_4 at low pressures and argon at all pressures), due to the unique electron power absorption dynamics induced by voltage waveform tailoring.

These findings are expected to have extremely important consequences for a variety of radio frequency plasma applications, for which CF_4 or other electronegative gases are typically used, as the DC self-bias and excitation/ionization dynamics strongly influence the formation of process relevant flux-energy distributions of all particle species, including electrons, ions, and neutrals.

Acknowledgments

The work described in this paper was made possible by financial support from the ANR projects APOCALYPSO (ANR-13-PRGE-0003-01), CleanGRAPH (ANR-13-BS09-0019), the UK EPSRC (EP/K018388/1 & EP/H003797/1), and the York-Paris Low Temperature Plasma Collaborative Research Centre. B Bruneau is also supported by the Doctoral School of Ecole Polytechnique (EDX grant, Ecole Doctorale de l'X). Support from the Hungarian Scientific Research Fund through the grant OTKA-K-105476 is gratefully acknowledged. M Koepke is supported by the NSF grant PHY-1301896. This work is part of a dissertation to be submitted by S Brandt to the Eberly College of Arts and Sciences, West Virginia University, Morgantown, WV, in partial fulfillment of the requirements for the PhD Degree in physics.

References

[1] Chu P K, Chen J Y, Wang L P and Huang N 2002 Plasma-surface modification of biomaterials *Mater. Sci. Eng.* R **36** 143
[2] Gomathi N, Sureshkumar A and Neogi S 2008 RF plasma-treated polymers for biomedical applications *Current Science* **94** 1478
[3] Fridman A and Friedman G 2013 *Plasma Medicine* 1st edn (Oxford: Wiley)
[4] Makabe T and Petrović Z 2006 *Plasma Electronics: Applications in Microelectronic Device Fabrication* (New York: Taylor & Francis)
[5] Donnelly V M and Kornblit A 2013 Plasma etching: yesterday, today, and tomorrow *J. Vac. Sci. Technol.* A **31** 050825
[6] Rath J 2003 Low temperature polycrystalline silicon: a review on deposition, physical properties and solar cell applications *Sol. Energy Mater. Sol. Cells* **76** 431
[7] Lee H-C, Bang J-Y and Chung C-W 2011 *Thin Solid Films* **519** 7009
[8] Lee H-C, Bang J-Y and Chung C-W 2012 *Appl. Phys. Lett.* **101** 244104
[9] Sobolewski M A and Kim J-H 2007 *J. Appl. Phys.* **102** 113302
[10] Schulze J, Schüngel E and Czarnetzki U 2012 *Appl. Phys. Lett.* **100** 024102
[11] Donkó Z, Schulze J, Czarnetzki U, Derzsi A, Hartmann P, Korolov I and Schüngel E 2012 Fundamental investigations of capacitive radio frequency plasmas: simulations and experiments *Plasma Phys. Control. Fusion* **54** 124003
[12] Schulze J, Gans T, O'Connell D, Czarnetzki U, Ellingboe A R and Turner M M 2007 Space and phase resolved plasma parameters in an industrial dual-frequency capacitively coupled radio-frequency discharge *J. Phys. D: Appl. Phys.* **40** 7008
[13] Waskoenig J and Gans T 2010 Nonlinear frequency coupling in dual radio-frequency driven atmospheric pressure plasmas *Appl. Phys. Lett.* **96** 181501
[14] Gans T, Schulze J, O'Connell D, Czarnetzki U, Faulkner R, Ellingboe A R and Turner M M 2006 Frequency coupling in dual frequency capacitively coupled radio-frequency plasmas *Appl. Phys. Lett.* **89** 261502
[15] Song S-H and Kushner M J 2012 Control of electron energy distributions and plasma characteristics of dual frequency, pulsed capacitively coupled plasmas sustained in Ar and $Ar/CF_4/O_2$ *Plasma Sources Sci. Technol.* **21** 055028
[16] Donkó Z, Schulze J, Hartmann P, Korolov I, Czarnetzki U and Schüngel E 2010 The effect of secondary electrons on the separate control of ion energy and flux in dual-frequency capacitively coupled radio frequency discharges *Appl. Phys. Lett.* **97** 081501
[17] Heil B G, Czarnetzki U, Brinkmann R P and Mussenbrock T 2008 On the possibility of making a geometrically symmetric RF-CCP discharge electrically asymmetric *J. Phys. D: Appl. Phys.* **41** 165202
[18] Donkó Z, Schulze J, Heil B G and Czarnetzki U 2009 PIC simulations of the separate control of ion flux and energy in CCRF discharges via the electrical asymmetry effect *J. Phys. D: Appl. Phys.* **42** 025205
[19] Schulze J, Schüngel E and Czarnetzki U 2009 The electrical asymmetry effect in capacitively coupled radio frequency discharges measurements of dc self bias, ion energy and ion flux *J. Phys. D: Appl. Phys.* **42** 092005
[20] Czarnetzki U, Schulze J, Schüngel E and Donkó Z 2011 The electrical asymmetry effect in capacitively coupled radio-frequency discharges *Plasma Sources Sci. Technol.* **20** 024010
[21] Bienholz S, Styrnoll T and Awakowicz P 2014 On the electrical asymmetry effect in large area multiple frequency

capacitively coupled plasmas *J. Phys. D: Appl. Phys.* **47** 065201
[22] Schüngel E, Schulze J, Donkó Z and Czarnetzki U 2011 Power absorption in electrically asymmetric dual frequency capacitive radio frequency discharges *Phys. Plasmas* **18** 013503
[23] Schulze J, Schüngel E, Donkó Z and Czarnetzki U 2010 Excitation dynamics in electrically asymmetric capacitively coupled radio frequency discharges: experiment, simulation, and model *Plasma Sources Sci. Technol.* **19** 045028
[24] Schüngel E, Eremin D, Schulze J, Mussenbrock T and Czarnetzki U 2012 The electrical asymmetry effect in geometrically asymmetric capacitive radio frequency plasmas *J. Appl. Phys.* **112** 053302
[25] Schulze J, Schüngel E, Donkó Z and Czarnetzki U 2011 The electrical asymmetry effect in multi-frequency capacitively coupled radio frequency discharges *Plasma Sources Sci. Technol.* **20** 015017
[26] Derzsi A, Korolov I, Schüngel E, Donkó Z and Schulze J 2013 Electron heating and control of ion properties in capacitive discharges driven by customized voltage waveforms *Plasma Sources Sci. Technol.* **22** 065009
[27] Zhang Y, Zafar A, Coumou D, Shannon S and Kushner M 2015 Control of ion energy distribution using phase shifting in multi-frequency capacitively coupled plasmas *J. Appl. Phys.* **117** 233302
[28] Gibson A R, Greb A, Graham W G and Gans T 2015 Tailoring the nonlinear frequency coupling between odd harmonics for the optimization of charged particle dynamics in capacitively coupled oxygen plasmas *Appl. Phys. Lett.* **106** 054102
[29] Bora B 2015 Effect of driving voltages in dual capacitively coupled radio frequency plasma: a study by nonlinear global model *Phys. Plasmas* **22** 103503
[30] Bora B 2015 Studies on the effect of finite geometrical asymmetry in dual capacitively coupled radio frequency plasma *Plasma Sources Sci. Technol.* **24** 054002
[31] Lafleur T, Delattre P A, Johnson E V and Booth J P 2012 Separate control of the ion flux and ion energy in capacitively coupled radio-frequency discharges using voltage waveform tailoring *Appl. Phys. Lett.* **101** 124104
[32] Lafleur T, Delattre P A, Johnson E V and Booth J P 2013 Capacitively coupled radio-frequency plasmas excited by tailored voltage waveforms *Plasma Phys. Control. Fusion* **55** 124002
[33] Coumou D J, Clark D H, Kummerer T, Hopkins M, Sullivan D and Shannon S 2014 Ion energy distribution skew control using phase-locked harmonic RF bias drive *IEEE Trans. Plasma Sci.* **42** 1880
[34] Qin X V, Ting Y-H and Wendt A E 2010 Tailored ion energy distributions at an RF-biased plasma electrode *Plasma Sources Sci. Technol.* **19** 065014
[35] Bruneau B, Lafleur T, Booth J P and Johnson E 2016 Controlling the shape of the ion energy distribution at constant ion flux and constant mean ion energy with tailored voltage waveforms *Plasma Sources Sci. Technol.* **25** 025006
[36] Schüngel E, Donkó Z, Hartmann P, Derzsi A, Korolov I and Schulze J 2015 Customized ion flux-energy distribution functions in capacitively coupled plasmas by voltage waveform tailoring *Plasma Sources Sci. Technol.* **24** 045013
[37] O'Neill C, Waskoenig J and Gans T 2012 Tailoring electron energy distribution functions through energy confinement in dual radio-frequency driven atmospheric pressure plasmas *Appl. Phys. Lett.* **101** 154107
[38] O'Connell D, Gans T, Semmler E and Awakowicz P 2008 The role of the relative voltage and phase for frequency coupling in a dual-frequency capacitively coupled plasma *Appl. Phys. Lett.* **93** 081502
[39] Diomede P, Economou D J, Lafleur T, Booth J P and Longo S 2014 Radio-frequency capacitively coupled plasmas in hydrogen excited by tailored voltage waveforms: comparison of simulations with experiments *Plasma Sources Sci. Technol.* **23** 065049
[40] Schüngel E, Mohr S, Iwashita S, Schulze J and Czarnetzki U 2013 The effect of dust on electron heating and dc self-bias in hydrogen diluted silane discharges *J. Phys. D: Appl. Phys.* **46** 175205
[41] Schulze J, Derzsi A and Donkó Z 2011 Electron heating and the electrical asymmetry effect in dual-frequency capacitive CF_4 discharges *Plasma Sources Sci. Technol.* **20** 045008
[42] Johnson E V, Verbeke T, Vanel J-C and Booth J-P 2010 Nanocrystalline silicon film growth morphology control through RF waveform tailoring *J. Phys. D: Appl. Phys.* **43** 412001
[43] Johnson E V, Delattre P A and Booth J-P 2012 Microcrystalline silicon solar cells deposited using a plasma process excited by tailored voltage waveforms *Appl. Phys. Lett.* **100** 133504
[44] Johnson E V, Pouliquen S, Delattre P A and Booth J-P 2012 Hydrogenated microcrystalline silicon thin films deposited by RF-PECVD under low ion bombardment energy using voltage waveform tailoring *J. Non-Cryst. Solids* **358** 1974
[45] Schüngel E, Hofmann R, Mohr S, Schulze J, Röpcke J and Czarnetzki U 2015 Evaluation of the electrical asymmetry effect by spectroscopic measurements of capacitively coupled discharges and silicon thin film depositions *Thin Solid Films* **574** 60
[46] Schüngel E, Mohr S, Schulze J and Czarnetzki U 2015 Prevention of lateral ion flux inhomogneities in large area capacitive radio frequency plasmas via the electrical asymmetry effect *Appl. Phys. Lett.* **106** 054108
[47] Franek J, Brandt S, Berger B, Liese M, Barthel M, Schüngel E and Schulze J 2015 Power supply and impedance matching to drive technological radio-frequency plasmas with customized voltage waveforms *Rev. Sci. Instrum.* **86** 053504
[48] Schüngel E, Brandt S, Korolov I, Derzsi A, Donkó Z and Schulze J 2015 On the self-excitation mechanisms of plasma series resonance oscillations in single- and multi-frequency capacitive discharges *Phys. Plasmas* **22** 043512
[49] Bruneau B, Novikova T, Lafleur T, Booth J P and Johnson E V 2015 Control and optimization of the slope asymmetry effect in tailored voltage waveforms for capacitively coupled plasmas *Plasma Sources Sci. Technol.* **24** 015021
[50] Bruneau B, Novikova T, Lafleur T, Booth J P and Johnson E V 2014 Ion flux asymmetry in radiofrequency capacitively-coupled plasmas excited by sawtooth-like waveforms *Plasma Sources Sci. Technol.* **23** 065010
[51] Bruneau B, Gans T, O'Connell D, Greb A, Johnson E V and Booth J P 2015 Strong ionization asymmetry in a geometrically symmetric radio frequency capacitively coupled plasma induced by sawtooth voltage waveforms *Phys. Rev. Lett.* **114** 125002
[52] Bruneau B *et al* 2016 Effect of gas properties on the dynamics of the electrical slope asymmetry effect in capacitive plasmas: comparison of Ar, H_2 and CF_4 *Plasma Sources Sci. Technol.* **25** 01LT02
[53] Belenguer Ph and Boeuf J P 1990 Transition between different regimes of RF glow discharges *Phys. Rev.* A **41** 4447
[54] Schulze J, Donkó Z, Luggenhölscher D and Czarnetzki U 2009 Different modes of electron heating in dual-frequency capacitively coupled radio frequency discharges *Plasma Sources Sci. Technol.* **18** 034011
[55] Schulze J, Heil B G, Luggenhölscher D, Brinkmann R P and Czarnetzki U 2008 Stochastic heating in asymmetric

capacitively coupled RF discharges *J. Phys. D: Appl. Phys.* **41** 195212
[56] Gozadinos G, Turner M M and Vender D 2001 Collisionless electron heating by capacitive RF sheaths *Phys. Rev. Lett.* **87** 135004
[57] Tatanova M, Golubovskii Yu B, Smirnov A S, Seimer G, Basner R and Kersten H 2009 Electron stochastic heating in a capacitively coupled low-pressure argon RF-discharge *Plasma Sources Sci. Technol.* **18** 025026
[58] Czarnetzki U, Heil B G, Schulze J, Donkó Z, Mussenbrock T and Brinkmann R P 2009 The electrical asymmetry effect—a novel and simple method for separate control of ion energy and flux in capacitively coupled RF discharges *J. Phys.: Conf. Ser.* **162** 012010
[59] Schulze J, Derzsi A, Dittmann K, Hemke T, Meichnser J and Donkó Z 2011 Ionization by drift and ambipolar electric fields in electronegative capacitive radio frequency plasmas *Phys. Rev. Lett.* **107** 275001
[60] Tochikubo F, Suzuki A, Kakuta S, Terazono Y and Makabe T 1990 Study of the structure in RF glow discharges in SiH_4/H_2 by spatiotemporal optical emission spectroscopy: influence of negative ions *J. Appl. Phys.* **68** 5532
[61] Küllig C, Dittmann K, Wegner T, Sheykin I, Matyash K, Loffhagen D, Schneider R and Meichsner J 2012 Dynamics and electronegativity of oxygen RF plasmas *Contrib. Plasma Phys.* **52** 836
[62] Boeuf J P and Belenguer Ph 1992 Transition from a capacitive to a resistive regime in a silane radio frequency discharge and its possible relation to powder formation *J. Appl. Phys.* **71** 4751
[63] Liu G-H, Liu Y-X, Wen D-Q and Wang Y-N 2015 Heating mode transition in capacitively coupled CF_4 discharges: comparison of experiments with simulations *Plasma Sources Sci. Technol.* **24** 034006
[64] Zhang Q-Z, Wang Y-N and Bogaerts A 2014 Heating mode transition in a hybrid direct current/dual-frequency capacitively coupled CF_4 discharge *J. Appl. Phys.* **115** 223302
[65] Hemke T, Eremin D, Mussenbrock T, Derzsi A, Donkó Z, Dittmann K, Meichsner J and Schulze J 2013 Ionization by bulk heating of electrons in capacitive radio frequency atmospheric pressure microplasmas *Plasma Sources Sci. Technol.* **22** 015012
[66] Dittmann K, Matyash K, Nemschokmichal S, Meichsner J and Schneider R 2010 Excitation mechanisms and sheath dynamics in capacitively coupled radio-frequency oxygen plasmas *Contrib. Plasma Phys.* **50** 942
[67] Gans T, O'Connell D, Schulz-von der Gathen V and Waskoenig J 2010 The challenge of revealing and tailoring the dynamics of radio-frequency plasmas *Plasma Sources Sci. Technol.* **19** 034010
[68] Mahony C M O, Al Wazzan R and Graham W G 1997 Sheath dynamics observed in a 13.56 MHz-driven plasma *Appl. Phys. Lett.* **71** 608
[69] Schulze J, Donkó Z, Heil B G, Luggenhölscher D, Mussenbrock T, Brinkmann R P and Czarnetzki U 2008 Electric field reversals in the sheath region of capacitively coupled radio frequency discharges at different pressures *J. Phys. D: Appl. Phys.* **41** 105214
[70] Czarnetzki U, Luggenhölscher D and Döbele H F 1999 Space and time resolved electric field measurements in helium and hydrogen RF-discharges *Plasma Sources Sci. Technol.* **8** 230
[71] Lieberman M A and Godyak V A 1998 From Fermi acceleration to collisionless discharge heating *IEEE Trans. Plasma Sci.* **26** 955
[72] Surendra M and Graves D B 1991 Electron acoustic waves in capacitively coupled, low-pressure RF glow discharges *Phys. Rev. Lett.* **66** 1469
[73] Salabas A, Marques L, Jolly J and Alves L L 2004 Systematic characterization of low-pressure capacitively coupled hydrogen discharges *J. Appl. Phys.* **95** 4605
[74] Vender D and Boswell R W 1990 Numerical modeling of low-pressure RF plasmas *IEEE Trans. Plasma Sci.* **18** 725
[75] Killer C, Bandelow G, Matyash K, Schneider R and Melzer A 2013 Observation of X mode electron heating in dusty argon radio frequency discharges *Phys. Plasmas* **20** 083704
[76] Lafleur T, Chabert P and Booth J P 2014 Electron heating in capacitively coupled plasmas revisited *Plasma Sources Sci. Technol.* **23** 035010
[77] Schulze J, Schüngel E, Derzsi A, Korolov I, Mussenbrock T and Donkó Z 2014 Complex electron heating in capacitive multi-frequency plasmas *IEEE Trans. Plasma Sci.* **42** 2780
[78] Schulze J, Donkó Z, Derzsi A, Korolov I and Schüngel E 2015 The effect of ambipolar electric fields on the electron heating in capacitive RF plasmas *Plasma Sources Sci. Technol.* **24** 015019
[79] Tochikubo F, Makabe T, Kakuta S and Suzuki A 1992 Study of the structure of radio-frequency glow-discharges in CH_4 and H_2 by spatiotemporal optical-emission spectroscopy *J. Appl. Phys.* **71** 2143
[80] Radovanov S B, Dzierzega K, Roberts J R and Olthoff J K 1995 Time-resolved Balmer-alpha emission from fast hydrogen atoms in low pressure, radio-frequency discharges in hydrogen *Appl. Phys. Lett.* **66** 2637
[81] Coburn J W and Kay E 1972 Positive-ion bombardment of substrates in RF diode glow discharge sputtering *J. Appl. Phys.* **43** 4965
[82] Lieberman M A and Savas S E 1990 Bias voltage in finite length, cylindrical and coaxial radio-frequency discharges *J. Vac. Sci. Technol.* A **8** 1632
[83] Schulze J, Schuengel E, Donkó Z, Luggenhoelscher D and Czarnetzki U 2010 Phase resolved optical emission spectroscopy: a non-intrusive diagnostic to study electron dynamics in capacitive radio frequency discharges *J. Phys. D: Appl. phys.* **43** 124016
[84] Böhm C and Perrin J 1991 Spatially resolved optical emission and electrical properties of SiH_4 RF discharges at 13.56 MHz in a symmetric parallel-plate configuration *J. Phys. D: Appl. Phys.* **24** 865
[85] Greb A, Gibson A R, Niemi K, O'Connell D and Gans T 2015 Influence of surface conditions on plasma dynamics and electron heating in a radio-frequency driven capacitively coupled oxygen plasma *Plasma Sources Sci. Technol.* **24** 044003
[86] Wise L W, Smith M W, Glennon B M, Lidén K and NIST ASD Team 2014 *NIST Atomic Spectra Database (ver. 5.2)* (Gaithersburg, MD: National Institute of Standards and Technology) [online] available: http://physics.nist.gov/asd
[87] Birdsall C K 1991 Particle-in-cell charged-particle simulations, plus Monte Carlo collisions with neutral atoms, PIC-MCC *IEEE Trans. Plasma Science* **19** 65
[88] Verboncoeur J P 2005 Particle simulation of plasmas: review and advances *Plasma Phys. Control. Fusion* **47** A231
[89] Matyash K, Schneider R, Taccogna F, Hatayama A, Longo S, Capitelli M, Tskhakaya D and Bronold F X 2007 Particle in cell simulation of low temperature laboratory plasmas *Contrib. Plasma Phys.* **47** 595
[90] Kurihara M, Petrović Z Lj and Makabe T 2000 Transport coefficients and scattering cross-sections for plasma modelling in CF_4-Ar mixtures: a swarm analysis *J. Phys. D: Appl. Phys.* **33** 2146
[91] Bonham R A 1994 Electron impact cross section data for carbon tetraflouride *Japan J. Appl. Phys.* **33** 4157
[92] Georgieva V, Bogaerts A and Gijbels R 2003 Numerical study of $Ar/CF_4/N_2$ discharges in single- and

dual-frequency capacitively coupled plasma reactors *J. Appl. Phys.* **93** 2369
[93] Georgieva V, Bogaerts A and Gijbels R 2004 *J. Appl. Phys.* **94** 3748
[94] Georgieva V, Bogaerts A and Gijbels R 2004 Numerical investigation of ion-energy-distribution functions in single and dual frequency capacitively coupled plasma reactors *Phys. Rev.* E **69** 026406
[95] Nanbu K 2000 Probability theory of electron-molecule, ion-molecule, molecule-molecule, and Coulomb collisions for particle modellling of materials processing plasmas and gases *IEEE Trans. Plasma Sci.* **28** 971
[96] Ehlerding A *et al* 2006 The dissociative recombination of fluorocarbon ions III: CF_2^+ and CF_3^+ *J. Phys. B: At. Mol. Opt. Phys.* **39** 805
[97] Morris R A, Viggiano A A, Van Doren J M and Paulson J F 1992 Chemistry of CF_n^+ ($n = 1$–3) ions with halocarbons *J. Phys. Chem.* **96** 2597
[98] Nanbu K and Denpoh K 1998 Monte Carlo collision simulation of positive-negative ion recombination for a given rate constant *J. Phys. Soc. Japan* **67** 1288
[99] Proshina O V, Rakhimova T V, Rakhimov A T and Voloshin D G 2010 Two modes of capacitively coupled RF discharge in CF_4 *Plasma Sources Sci. Technol.* **19** 065013
[100] Denpoh K and Nanbu K 2000 Self-consistent particle simulation of radio frequency CF_4 discharge: effect of gas pressure *Japan J. Appl. Phys.* **39** 2804
[101] Kollath R 1956 *Encyclopedia of Physics* vol 21, ed S Flügge (Berlin: Springer) p 264